Research Article | Vol. 8, No. 11 | 1 Nov 2017 | BIOMEDICAL OPTICS EXPRESS 5049
Biomedical Optics EXPRESS

Automated drusen detection in dry age-related macular degeneration by multiple-depth, *en face* optical coherence tomography

Rui Zhao,[1,2,3] Acner Camino,[1,3] Jie Wang,[1] Ahmed M. Hagag,[1] Yansha Lu,[1,2] Steven T. Bailey,[1] Christina J. Flaxel,[1] Thomas S. Hwang,[1] David Huang,[1] Dengwang Li,[2,4] and Yali Jia[1,5]

[1]*Casey Eye Institute, Oregon Health & Science University, Portland, OR, 27239, USA*
[2]*Shandong Province Key Laboratory of Medical Physics and Image Processing Technology, School of Physics and Electronics, Shandong Normal University, Jinan, 250014, China*
[3]*These authors contributed equally to this work*
[4]*dengwang@sdnu.edu.cn*
[5]*jiaya@ohsu.edu*

Abstract: We introduce a method to automatically detect drusen in dry age-related macular degeneration (AMD) from optical coherence tomography with minimum need for layer segmentation. The method is based on the *en face* detection of drusen areas in C-scans at certain distances above the Bruch's membrane, circumventing the difficult task of pathologic retinal pigment epithelium segmentation. All types of drusen can be detected, including the challenging subretinal drusenoid deposits (pseudodrusen). The high sensitivity and accuracy demonstrated here shows its potential for detection of drusen onset in early AMD.

OCIS codes: (170.4500) Optical coherence tomography; (170.4470) Ophthalmology; (100.6890) Three-dimensional image processing; (170.1610) Clinical applications.

References and links

1. D. C. Neely, K. J. Bray, C. E. Huisingh, M. E. Clark, G. McGwin, Jr., and C. Owsley, "Prevalence of Undiagnosed Age-Related Macular Degeneration in Primary Eye Care," JAMA Ophthalmol. **135**(6), 570–575 (2017).
2. D. Pascolini and S. P. Mariotti, "Global estimates of visual impairment: 2010," Br. J. Ophthalmol. **96**(5), 614–618 (2012).
3. W. L. Wong, X. Su, X. Li, C. M. Cheung, R. Klein, C. Y. Cheng, and T. Y. Wong, "Global prevalence of age-related macular degeneration and disease burden projection for 2020 and 2040: a systematic review and meta-analysis," Lancet Glob. Health **2**(2), e106–e116 (2014).
4. H. Müller, "Anatomische Beiträge zur Ophthalmologie," Arch. Ophthalmol. **2**, 1–69 (1856).
5. L. Wang, M. E. Clark, D. K. Crossman, K. Kojima, J. D. Messinger, J. A. Mobley, and C. A. Curcio, "Abundant Lipid and Protein Components of Drusen," PLoS One **5**(4), e10329 (2010).
6. N. M. Bressler, S. B. Bressler, and S. L. Fine, "Age-related macular degeneration," Surv. Ophthalmol. **32**(6), 375–413 (1988).
7. S. A. Zweifel, R. F. Spaide, C. A. Curcio, G. Malek, and Y. Imamura, "Reticular pseudodrusen are subretinal drusenoid deposits," Ophthalmology **117**(2), 303–312.e1, e301 (2010).
8. S. Boddu, M. D. Lee, M. Marsiglia, M. Marmor, K. B. Freund, and R. T. Smith, "Risk factors associated with reticular pseudodrusen versus large soft drusen," Am. J. Ophthalmol. **157**(5), 985–993.e2, e982 (2014).
9. R. P. Finger, Z. Wu, C. D. Luu, F. Kearney, L. N. Ayton, L. M. Lucci, W. C. Hubbard, J. L. Hageman, G. S. Hageman, and R. H. Guymer, "Reticular pseudodrusen: a risk factor for geographic atrophy in fellow eyes of individuals with unilateral choroidal neovascularization," Ophthalmology **121**(6), 1252–1256 (2014).
10. Y. Kanagasingam, A. Bhuiyan, M. D. Abràmoff, R. T. Smith, L. Goldschmidt, and T. Y. Wong, "Progress on retinal image analysis for age related macular degeneration," Prog. Retin. Eye Res. **38**, 20–42 (2014).
11. J. J. Arnold, S. H. Sarks, M. C. Killingsworth, and J. P. Sarks, "Reticular pseudodrusen. A risk factor in age-related maculopathy," Retina **15**(3), 183–191 (1995).
12. R. T. Smith, J. K. Chan, M. Busuoic, V. Sivagnanavel, A. C. Bird, and N. V. Chong, "Autofluorescence characteristics of early, atrophic, and high-risk fellow eyes in age-related macular degeneration," Invest. Ophthalmol. Vis. Sci. **47**(12), 5495–5504 (2006).
13. D. S. Shin, N. B. Javornik, and J. W. Berger, "Computer-assisted, interactive fundus image processing for macular drusen quantitation," Ophthalmology **106**(6), 1119–1125 (1999).

#305458 https://doi.org/10.1364/BOE.8.005049
Journal © 2017 Received 23 Aug 2017; revised 14 Sep 2017; accepted 12 Oct 2017; published 17 Oct 2017

Biomedical Optics EXPRESS

14. K. Rapantzikos, M. Zervakis, and K. Balas, "Detection and segmentation of drusen deposits on human retina: potential in the diagnosis of age-related macular degeneration," Med. Image Anal. **7**(1), 95–108 (2003).
15. C. Köse, U. Sevik, and O. Gençalioğlu, "Automatic segmentation of age-related macular degeneration in retinal fundus images," Comput. Biol. Med. **38**(5), 611–619 (2008).
16. M. J. van Grinsven, Y. T. Lechanteur, J. P. van de Ven, B. van Ginneken, C. B. Hoyng, T. Theelen, and C. I. Sánchez, "Automatic drusen quantification and risk assessment of age-related macular degeneration on color fundus images," Invest. Ophthalmol. Vis. Sci. **54**(4), 3019–3027 (2013).
17. H. Bartlett and F. Eperjesi, "Use of fundus imaging in quantification of age-related macular change," Surv. Ophthalmol. **52**(6), 655–671 (2007).
18. R. T. Smith, J. K. Chan, T. Nagasaki, J. R. Sparrow, and I. Barbazetto, "A method of drusen measurement based on reconstruction of fundus background reflectance," Br. J. Ophthalmol. **89**(1), 87–91 (2005).
19. A. von Rückmann, F. W. Fitzke, and A. C. Bird, "Distribution of fundus autofluorescence with a scanning laser ophthalmoscope," Br. J. Ophthalmol. **79**(5), 407–412 (1995).
20. R. T. Smith, M. A. Sohrab, M. Busuioc, and G. Barile, "Reticular macular disease," Am. J. Ophthalmol. **148**(5), 733–743.e2, e732 (2009).
21. A. Ly, L. Nivison-Smith, N. Assaad, and M. Kalloniatis, "Fundus Autofluorescence in Age-related Macular Degeneration," Optom. Vis. Sci. **94**(2), 246–259 (2017).
22. J. H. Acton, R. P. Cubbidge, H. King, P. Galsworthy, and J. M. Gibson, "Drusen detection in retro-mode imaging by a scanning laser ophthalmoscope," Acta Ophthalmol. **89**(5), e404–e411 (2011).
23. R. F. Spaide and C. A. Curcio, "Drusen Characterization with Multimodal Imaging," Retina **30**(9), 1441–1454 (2010).
24. M. Anderson, W. W. Dawson, J. Gonzalez-Martinez, and C. A. Curcio, "Drusen and lipid-filled retinal pigment epithelium cells in a rhesus macula," Vet. Ophthalmol. **9**(3), 201–207 (2006).
25. A. D. Mora, P. M. Vieira, A. Manivannan, and J. M. Fonseca, "Automated drusen detection in retinal images using analytical modelling algorithms," Biomed. Eng. Online **10**, 59 (2011).
26. C. Köse, U. Sevik, O. Gençalioğlu, C. Ikibaş, and T. Kayikiçioğlu, "A statistical segmentation method for measuring age-related macular degeneration in retinal fundus images," J. Med. Syst. **34**(1), 1–13 (2010).
27. E. A. Swanson, J. A. Izatt, M. R. Hee, D. Huang, C. P. Lin, J. S. Schuman, C. A. Puliafito, and J. G. Fujimoto, "In vivo retinal imaging by optical coherence tomography," Opt. Lett. **18**(21), 1864–1866 (1993).
28. D. Huang, E. A. Swanson, C. P. Lin, J. S. Schuman, W. G. Stinson, W. Chang, M. R. Hee, T. Flotte, K. Gregory, C. A. Puliafito, and J. G. Fujimoto, "Optical coherence tomography," Science **254**(5035), 1178–1181 (1991).
29. B. Baumann, E. Götzinger, M. Pircher, H. Sattmann, C. Schütze, F. Schlanitz, C. Ahlers, U. Schmidt-Erfurth, and C. K. Hitzenberger, "Segmentation and quantification of retinal lesions in age-related macular degeneration using polarization-sensitive optical coherence tomography," J. Biomed. Opt. **15**, 061704 (2010).
30. F. G. Schlanitz, C. Ahlers, S. Sacu, C. Schütze, M. Rodriguez, S. Schriefl, I. Golbaz, T. Spalek, G. Stock, and U. Schmidt-Erfurth, "Performance of drusen detection by spectral-domain optical coherence tomography," Invest. Ophthalmol. Vis. Sci. **51**(12), 6715–6721 (2010).
31. Q. Chen, T. Leng, L. Zheng, L. Kutzscher, J. Ma, L. de Sisternes, and D. L. Rubin, "Automated drusen segmentation and quantification in SD-OCT images," Med. Image Anal. **17**(8), 1058–1072 (2013).
32. N. Jain, S. Farsiu, A. A. Khanifar, S. Bearelly, R. T. Smith, J. A. Izatt, and C. A. Toth, "Quantitative Comparison of Drusen Segmented on SD-OCT versus Drusen Delineated on Color Fundus Photographs," Invest. Ophthalmol. Vis. Sci. **51**(10), 4875–4883 (2010).
33. Z. M. Dong, G. Wollstein, and J. S. Schuman, "Clinical Utility of Optical Coherence Tomography in Glaucoma," Invest. Ophthalmol. Vis. Sci. **57**(9), OCT556–OCT567 (2016).
34. I. I. Bussel, G. Wollstein, and J. S. Schuman, "OCT for glaucoma diagnosis, screening and detection of glaucoma progression," Br. J. Ophthalmol. **98**(Suppl 2), ii15–ii19 (2014).
35. G. Trichonas and P. K. Kaiser, "Optical coherence tomography imaging of macular oedema," Br. J. Ophthalmol. **98**(Suppl 2), ii24–ii29 (2014).
36. M. R. Hee, C. R. Baumal, C. A. Puliafito, J. S. Duker, E. Reichel, J. R. Wilkins, J. G. Coker, J. S. Schuman, E. A. Swanson, and J. G. Fujimoto, "Optical coherence tomography of age-related macular degeneration and choroidal neovascularization," Ophthalmology **103**(8), 1260–1270 (1996).
37. Q. Chen, T. Leng, L. Zheng, L. Kutzscher, J. Ma, L. de Sisternes, and D. L. Rubin, "Automated drusen segmentation and quantification in SD-OCT images," Med. Image Anal. **17**(8), 1058–1072 (2013).
38. S. J. C. Sina Farsiu A. J. Izatt, and C. A. Toth,Proc. SPIE 6844, Ophthalmic Technologies XVIII, 68440D (2008/02/11), "Fast detection and segmentation of drusen in retinal optical coherence tomography images," Proc. SPIE 6844, Ophthalmic Technologies **XVIII**, 68440D (2008).
39. K. Yi, M. Mujat, B. H. Park, W. Sun, J. W. Miller, J. M. Seddon, L. H. Young, J. F. de Boer, and T. C. Chen, "Spectral domain optical coherence tomography for quantitative evaluation of drusen and associated structural changes in non-neovascular age-related macular degeneration," Br. J. Ophthalmol. **93**(2), 176–181 (2009).
40. Q. Yang, C. A. Reisman, Z. Wang, Y. Fukuma, M. Hangai, N. Yoshimura, A. Tomidokoro, M. Araie, A. S. Raza, D. C. Hood, and K. Chan, "Automated layer segmentation of macular OCT images using dual-scale gradient information," Opt. Express **18**(20), 21293–21307 (2010).
41. S. J. Chiu, J. A. Izatt, R. V. O'Connell, K. P. Winter, C. A. Toth, and S. Farsiu, "Validated automatic segmentation of AMD pathology including drusen and geographic atrophy in SD-OCT images," Invest. Ophthalmol. Vis. Sci. **53**(1), 53–61 (2012).

Biomedical Optics EXPRESS

42. M. Zhang, J. Wang, A. D. Pechauer, T. S. Hwang, S. S. Gao, L. Liu, L. Liu, S. T. Bailey, D. J. Wilson, D. Huang, and Y. Jia, "Advanced image processing for optical coherence tomographic angiography of macular diseases," Biomed. Opt. Express **6**(12), 4661–4675 (2015).
43. F. Rathke, M. Desana, and C. Schnörr, "Locally Adaptive Probabilistic Models for Global Segmentation of Pathological OCT Scans," in *Proc. MICCAI*, 2017)
44. L. Fang, D. Cunefare, C. Wang, R. H. Guymer, S. Li, and S. Farsiu, "Automatic segmentation of nine retinal layer boundaries in OCT images of non-exudative AMD patients using deep learning and graph search," Biomed. Opt. Express **8**(5), 2732–2744 (2017).
45. S. Farsiu, S. J. Chiu, R. V. O'Connell, F. A. Folgar, E. Yuan, J. A. Izatt, and C. A. Toth; Age-Related Eye Disease Study 2 Ancillary Spectral Domain Optical Coherence Tomography Study Group, "Quantitative Classification of Eyes with and without Intermediate Age-related Macular Degeneration Using Optical Coherence Tomography," Ophthalmology **121**(1), 162–172 (2014).
46. G. Gregori, F. Wang, P. J. Rosenfeld, Z. Yehoshua, N. Z. Gregori, B. J. Lujan, C. A. Puliafito, and W. J. Feuer, "Spectral Domain Optical Coherence Tomography Imaging of Drusen in Nonexudative Age-Related Macular Degeneration," Ophthalmology **118**(7), 1373–1379 (2011).
47. L. de Sisternes, G. Jonna, M. A. Greven, Q. Chen, T. Leng, and D. L. Rubin, "Individual Drusen Segmentation and Repeatability and Reproducibility of Their Automated Quantification in Optical Coherence Tomography Images," Transl. Vis. Sci. Technol. **6**(1), 12 (2017).
48. M. F. Kraus, B. Potsaid, M. A. Mayer, R. Bock, B. Baumann, J. J. Liu, J. Hornegger, and J. G. Fujimoto, "Motion correction in optical coherence tomography volumes on a per A-scan basis using orthogonal scan patterns," Biomed. Opt. Express **3**(6), 1182–1199 (2012).
49. M. F. Kraus, J. J. Liu, J. Schottenhamml, C. L. Chen, A. Budai, L. Branchini, T. Ko, H. Ishikawa, G. Wollstein, J. Schuman, J. S. Duker, J. G. Fujimoto, and J. Hornegger, "Quantitative 3D-OCT motion correction with tilt and illumination correction, robust similarity measure and regularization," Biomed. Opt. Express **5**(8), 2591–2613 (2014).
50. E. N. Mortensen and W. A. Barrett, "Intelligent scissors for image composition," in *Proceedings of the 22nd annual conference on Computer graphics and interactive techniques,* (ACM, 1995), pp. 191–198.
51. C. Dongye, M. Zhang, T. S. Hwang, J. Wang, S. S. Gao, L. Liu, D. Huang, D. J. Wilson, and Y. Jia, "Automated detection of dilated capillaries on optical coherence tomography angiography," Biomed. Opt. Express **8**(2), 1101–1109 (2017).
52. M. A. Guerroudji and Z. Ameur, "A new approach for the detection of mammary calcifications by using the white Top-Hat transform and thresholding of Otsu," Optik - International Journal for Light and Electron Optics **127**, 1251– 1259 (2016).
53. Y. Jia, O. Tan, J. Tokayer, B. Potsaid, Y. Wang, J. J. Liu, M. F. Kraus, H. Subhash, J. G. Fujimoto, J. Hornegger, and D. Huang, "Split-spectrum amplitude-decorrelation angiography with optical coherence tomography," Opt. Express **20**(4), 4710–4725 (2012).
54. A. Camino, M. Zhang, S. S. Gao, T. S. Hwang, U. Sharma, D. J. Wilson, D. Huang, and Y. Jia, "Evaluation of artifact reduction in optical coherence tomography angiography with real-time tracking and motion correction technology," Biomed. Opt. Express **7**(10), 3905–3915 (2016).
55. J. Wang, M. Zhang, T. S. Hwang, S. T. Bailey, D. Huang, D. J. Wilson, and Y. Jia, "Reflectance-based projection-resolved optical coherence tomography angiography [Invited]," Biomed. Opt. Express **8**(3), 1536–1548 (2017).
56. J. P. Campbell, M. Zhang, T. S. Hwang, S. T. Bailey, D. J. Wilson, Y. Jia, and D. Huang, "Detailed Vascular Anatomy of the Human Retina by Projection-Resolved Optical Coherence Tomography Angiography," Sci. Rep. **7**, 42201 (2017).
57. Y. Jia, S. T. Bailey, T. S. Hwang, S. M. McClintic, S. S. Gao, M. E. Pennesi, C. J. Flaxel, A. K. Lauer, D. J. Wilson, J. Hornegger, J. G. Fujimoto, and D. Huang, "Quantitative optical coherence tomography angiography of vascular abnormalities in the living human eye," Proc. Natl. Acad. Sci. U.S.A. **112**(18), E2395–E2402 (2015).
58. Z. Wu, L. N. Ayton, C. D. Luu, P. N. Baird, and R. H. Guymer, "Reticular Pseudodrusen in Intermediate Age-Related Macular Degeneration: Prevalence, Detection, Clinical, Environmental, and Genetic Associations," Invest. Ophthalmol. Vis. Sci. **57**(3), 1310–1316 (2016).
59. S. A. Zweifel, Y. Imamura, T. C. Spaide, T. Fujiwara, and R. F. Spaide, "Prevalence and Significance of Subretinal Drusenoid Deposits (Reticular Pseudodrusen) in Age-Related Macular Degeneration," Ophthalmology **117**(9), 1775–1781 (2010).
60. K. B. Schaal, A. D. Legarreta, W. J. Feuer, G. Gregori, Q. Cheng, J. E. Legarreta, M. K. Durbin, P. F. Stetson, S. Kubach, and P. J. Rosenfeld, "Comparison between Widefield En Face Swept-Source OCT and Conventional Multimodal Imaging for the Detection of Reticular Pseudodrusen," Ophthalmology **124**(2), 205–214 (2017).
61. N. Ueda-Arakawa, S. Ooto, A. Tsujikawa, K. Yamashiro, A. Oishi, and N. Yoshimura, "Sensitivity And Specificity Of Detecting Reticular Pseudodrusen In Multimodal Imaging In Japanese Patients," Retina **33**(3), 490–497 (2013).
62. A. Stankiewicz, T. Marciniak, A. Dąbrowski, M. Stopa, P. Rakowicz, and E. Marciniak, "Improving Segmentation of 3D Retina Layers Based on Graph Theory Approach for Low Quality OCT Images," in *Metrology and Measurement Systems,* (2016), p. 269.

Biomedical Optics EXPRESS

63. K. Lee, G. H. S. Buitendijk, H. Bogunovic, H. Springelkamp, A. Hofman, A. Wahle, M. Sonka, J. R. Vingerling, C. C. W. Klaver, and M. D. Abràmoff, "Automated Segmentability Index for Layer Segmentation of Macular SD-OCT Images," Transl. Vis. Sci. Technol. **5**(2), 14 (2016).
64. J. Mazzaferri, L. Beaton, G. Hounye, D. N. Sayah, and S. Costantino, "Open-source algorithm for automatic choroid segmentation of OCT volume reconstructions," Sci. Rep. **7**, 42112 (2017).
65. R. F. Mullins, M. N. Johnson, E. A. Faidley, J. M. Skeie, and J. Huang, "Choriocapillaris Vascular Dropout Related to Density of Drusen in Human Eyes with Early Age-Related Macular Degeneration," Invest. Ophthalmol. Vis. Sci. **52**(3), 1606–1612 (2011).
66. L. Toto, E. Borrelli, L. Di Antonio, P. Carpineto, and R. Mastropasqua, "Retinal vascular plexuses' changes in dry age-related macular degeneration, evaluated by means of optical coherence tomography angiography," Retina **36**(8), 1566–1572 (2016).
67. J. Ma, R. Desai, P. Nesper, M. Gill, A. Fawzi, and D. Skondra, "Optical Coherence Tomographic Angiography Imaging in Age-Related Macular Degeneration," Ophthalmol. Eye Dis. **9**, 1179172116686075 (2017).

1. Introduction

Age-related macular degeneration (AMD) is a degenerative retinal disease and a leading cause of vision loss in older adults [1, 2]. It is estimated that 196 million people worldwide will have AMD by 2020 [3], 5-15% of which would progress to the advanced stage of the disease. In the early stage, AMD is characterized by asymptomatic deposition of clustered extracellular byproducts of photoreceptor metabolism on the retinal pigment epithelium (RPE), known as drusen. As the disease progresses and drusen enlarges, the RPE degenerates to a state of geographic atrophy, causing the death of RPE cells and subsequent loss of photoreceptor cells and choriocapillaries. These early and intermediate stages are customarily referred to as dry AMD. The late stage, known as exudative or wet AMD is characterized by choroidal neovascularization (CNV), which typically conduces to irreversible lesions caused by leakage, i.e. subretinal and intraretinal fluid accumulation and RPE detachment. Although currently only the neovascular stage is treated by clinicians, early detection of dry AMD is vital to slow down the progression of the disease by intake of nutrition supplements as well as control of body weight and high-risk activities such as cigarette smoking.

Drusen was first discovered in the XIX century and its sedimentary nature was understood from very early [4]. It begins to buildup due to the progressive deterioration of the Bruch's-membrane's conductivity and is mainly composed by lipoproteins [5]. Based on its appearance and location in retinal images, drusen has been classified as cuticular, soft or subretinal drusenoid deposits; each posing its own challenges for their automated segmentation and quantification. Cuticular drusen is typically small with sharp borders, is located below the RPE and has not shown predictive value for disease evolution. Soft drusen, on the other hand, appears as a bigger lesion with blurred borders and has been associated with further progression to a later stage of AMD [6]. Subretinal drusenoid deposits (previously known as reticular pseudodrusen) are located between the retinal pigment epithelium (RPE) and the ellipsoid zone [7], are more prevalent in later age AMD onset [8], and have been associated with high prevalence of progression to a late AMD stage [9–12].

For many years, color fundus photography has been the gold standard for drusen imaging in dry AMD. This technique takes advantage of the pigmentation variation in the retinal fundus caused by accumulation of cholesterol, lipofuscin and other metabolic waste products [13–18] to visualize drusen. In this modality, cuticular drusen is observed as a densely packed, white colored arrangement, while soft drusen appears in white-yellow color as lower-contrast round structures with larger diameter. Subretinal drusenoid deposits, on the other hand, appear in a slightly whiter/blue color owing to its localization above the RPE. Despite the large field of view available in fundus photography, other imaging modalities have been used in attempts to overcome the challenges faced by this technique, namely inhomogeneous illumination and poor contrast that impede accurately discerning drusen boundaries. For instance, fluorescein angiography (FA), despite being a more invasive procedure that requires intravenous injection, can detect a larger amount of cuticular drusen spots than fundus photography [6]. However, evaluation based on FA images alone is confounded by some drusen that does not fluoresce and hence, FA is typically used together with fundus

Biomedical Optics EXPRESS

photography. On the other hand, a less invasive modality known as fundus auto fluorescence (FAF) relies on short wavelength excitation of the fluorophore N-retinylidene-N-retinylethanolamine (A2E) found in lipofuscin [19] and detection of subsequent tissue fluorescence by a confocal scanning laser ophthalmoscope. This technique can display soft drusen and subretinal drusenoid deposits, but the second cannot be detected in the central zone due to the blockage of the excitation light by macular pigment [20], and outside the central zone can be misidentified with other AMD phenotypes [21]. Yet another alternative modality is infrared scanning laser ophthalmoscopy, which has shown ability to detect a larger drusen quantity than fundus photography owing to the deeper penetration with reduced scattering, characteristic of the central wavelength of the light source used [22]. All of these technologies are two-dimensional (2D) in nature, not allowing analysis of drusen in the axial dimension. Their inability to observe slabs at different depths into the retinal tissue makes it difficult to differentiate drusen from confounding spots [23, 24].

Several semi-automated image-processing methods have been proposed to detect drusen location, number and size. In early works, researchers tried to first homogenize the background and then apply a thresholding scheme based on intensity distributions rather than single pixel intensity levels for drusen detection. For instance, Rapantzikos et al. [14] utilized a complex multi-level histogram equalization routine to enhance drusen contrast and incorporated a larger number of descriptors in order to achieve unsupervised detection. Alternatively, statistical differences of the texture of drusen vs healthy regions have been used to differentiate them [26]. On the other hand, region growing methods have been used to complete the drusen detected by a method that analyzed the collective behavior of pixel brightness in local regions of incrementing size [13] as well as to recognize the healthy retinal area rather than the drusen area in the inverse segmentation approach proposed by Ref [15]. More recently, machine learning has also been applied to drusen detection and classification [16]. For a more comprehensive comparison of the methods found in this extensive literature, we refer the reader to the informative review article in Ref [10].

A non-invasive alternative to display all types of drusen both *en face* and cross-sectionally is optical coherence tomography (OCT) [27–32]. Over the past 25 years, OCT has consolidated as the most versatile technology used in ophthalmic care. It has shown value in the diagnosis and assessment of vision-threatening ocular diseases such as glaucoma [33, 34], diabetic retinopathy (DR) [35], and AMD [36]. Unlike all of the 2D techniques mentioned above, OCT does allow depth-resolved analysis of retinal tissue. Logically, the methods developed for drusen detection on OCT images have exploited its three-dimensional (3D) nature. Generally, they heavily rely on the segmentation of the RPE in cross-sectional images of the retina (B-scans) and further generation of an estimated "healthy" baseline by interpolation methods [37, 38]. Several approaches have been proposed to solve the problem of accurately delineating the pathologic RPE boundary in an automated manner, based on active contours models (deformable spline) [39], dual-scale gradient maps [40], graph search [41, 42], probabilistic models [43] and more recently, deep learning [44]. Accurate detection of layer boundaries with irregular shape in diseased cases is a major line of active research in OCT image processing, but RPE segmentation errors still abound in current techniques. An additional challenge is the task of determining a reliable threshold that recognizes RPE segmentation elevations caused by actual drusen from healthy regions in all cases [45, 46]. In consequence, most of these methods can detect neither early drusen deposits that do not result in significant elevation of the RPE nor subretinal drusenoid deposits located above the RPE, and could even overestimate the size of drusen (Fig. 1). Only recently, one method based on retinal layer segmentation showed ability to detect all types of drusen, limited to elevations larger than 20 μm [47].

Biomedical Optics EXPRESS

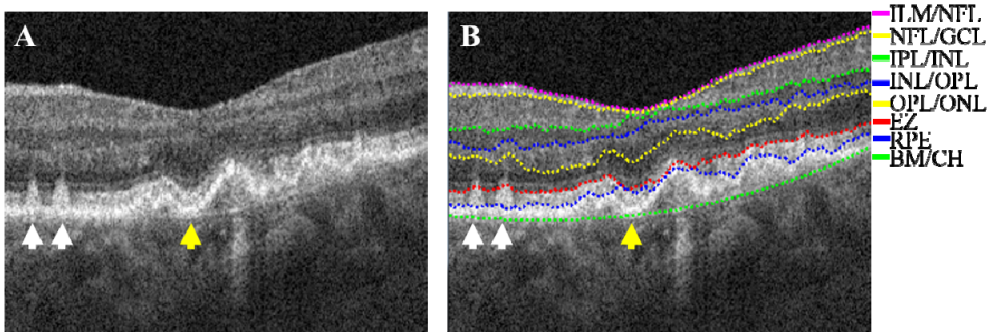

Fig. 1. Challenges faced by drusen detection from cross-sectional segmentation of the retinal pigment epithelium (RPE). (A) Representative cross-sectional scan. Subretinal drusenoid deposits are white arrows and a region of no elevation between two soft drusen domes is indicated by the yellow arrow. (B) Segmentation of eight retinal layer interfaces performed automatically without manual correction by an algorithm based on directional graph search [42]. According to the position detected for the inner RPE interface, drusen would be likely undetected at the white arrows due to minimal elevation of the interface and overestimated at the yellow arrow positions. ILM – Inner limiting membrane. NFL – Nerve fiber layer. GCL - Ganglion cell layer. IPL – Inner plexiform layer. INL – Inner nuclear layer. OPL – Outer plexiform layer. ONL – Outer nuclear layer. EZ – Ellipsoid zone of the photoreceptors. RPE – Retinal pigment epithelium. BM – Bruch's membrane. CH – choriocapillaris.

In this report, we introduce a highly sensitive drusen detection algorithm that uses C-scans contained in reflectance OCT slabs at different depths. This method does not need to perform delineation of the pathologic RPE boundary. By this approach, we can exploit OCT's three-dimensionality for the detection of all types of drusen while requiring segmentation of only the Bruch's membrane/choriocapillaris interface.

2. Data acquisition

Healthy participants and participants diagnosed with dry AMD were imaged at the Casey Eye Institute of Oregon Health & Science University (OHSU). All participants were enrolled after informed consent. The protocol was approved by the Institutional Review Board/Ethics Committee of OHSU, and adhered to the tenets of the Declaration of Helsinki.

A pair of successive volumetric scans acquired at orthogonal raster directions were collected from one eye of each participant two times by using a commercial spectral domain OCT system (RTVue-XR; Optovue, Fremont, CA). The instrument operates at a central wavelength of 840 nm, with a full-width half-maximum bandwidth of 45 nm and axial scan rate of 70 kHz. Each scan was captured in less than 3 seconds, which covers a 3×3 mm^2 area with a 2 mm depth, comprising a total of $304 \times 304 \times 2$ A-scans. The structural data was generated by averaging the two B-scans acquired consecutively at each scanning position. Then, each pair of volumetric scans underwent registration and merging by an eye motion correction algorithm incorporated in the Angiovue software [48, 49]. As a result, two motion-free data cubes containing reflectance OCT data of the retinal layers were obtained for each eye.

3. Algorithm

3.1 Overview

The algorithm was implemented using the Matlab 2013a release (Mathworks, Natick, MA, USA). Segmentation of the Bruch's membrane interface was automatically performed by a directional graph-search algorithm [42]. The drusen detection algorithm consisted of three main steps: pre-processing, drusen segmentation and post-processing (Fig. 2). The first step selects two slabs of seven C-scans each at different heights from the Bruch's membrane, homogenizes the background and increases the drusen contrast by averaging groups of three

Biomedical Optics EXPRESS

adjacent C-scans in the axial direction. In the drusen segmentation step, averaged C-scans at each slab undergo a dual-scale filtering scheme followed by Otsu thresholding that results in binary maps of the drusen area. Finally, the post-processing step consists of vessel shadow artifacts removal and subsequent smoothing of the detected drusen area. Each of these steps will be described in depth in the following sections.

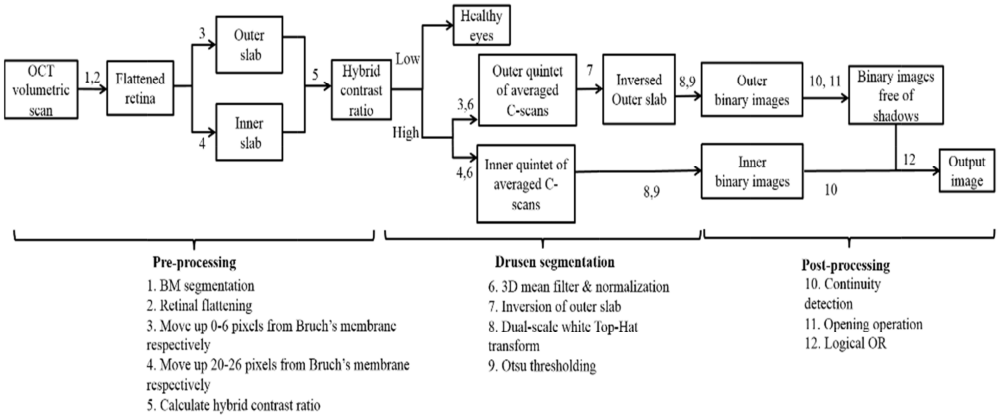

Fig. 2. Flow chart of the drusen detection algorithm.

3.2 Pre-processing step

Segmentation of only the Bruch's membrane was automatically performed on each B-scan of the reflectance OCT data by a directional graph search method [42] while the operator supervised the outcome. Manual correction guided by local graph search function could be done if necessary in custom processing software - the Center for Ophthalmic Optics & Lasers-Angiography Reading Toolkit (COOL-ART) [42, 50]. The segmentation on single B-frame could be propagated forward along subsequent B-scans. B-scan images were flattened to the detected boundary. Two slabs each containing seven C-scans were extracted after flattening, located at 0-6 pixels and 20-26 pixels above the Bruch's membrane respectively. One of the C-scans for each slab is represented in Fig. 3. In healthy eyes, these two slabs would be located respectively at the RPE and right above the ellipsoid zone (Fig. 3(A) and Fig. 4). In diseased eyes, soft drusen, cuticular drusen or subretinal drusenoid deposits can be found. In soft drusen, the C-scans of the outer slab appear dark in the regions with RPE elevation (Fig. 3(B) green arrow and Fig. 4) and bright elsewhere while in the C-scans of the inner slab, the drusen area is brighter than its surroundings. If the RPE outer boundary is above the inner slab, the inner slab will display black regions in the middle of soft drusen regions. Cuticular drusen appears dark in the outer slab and could be absent from C-scans in the inner slab when the EZ elevation is too marginal. Even when cuticular drusen reaches the inner slab, its size is usually smaller than in the outer slab due to their punctate appearance. Subretinal drusenoid deposits are located above the RPE and appear bright in both the inner and the outer slabs (Fig. 3(B), yellow arrows).

Biomedical Optics EXPRESS

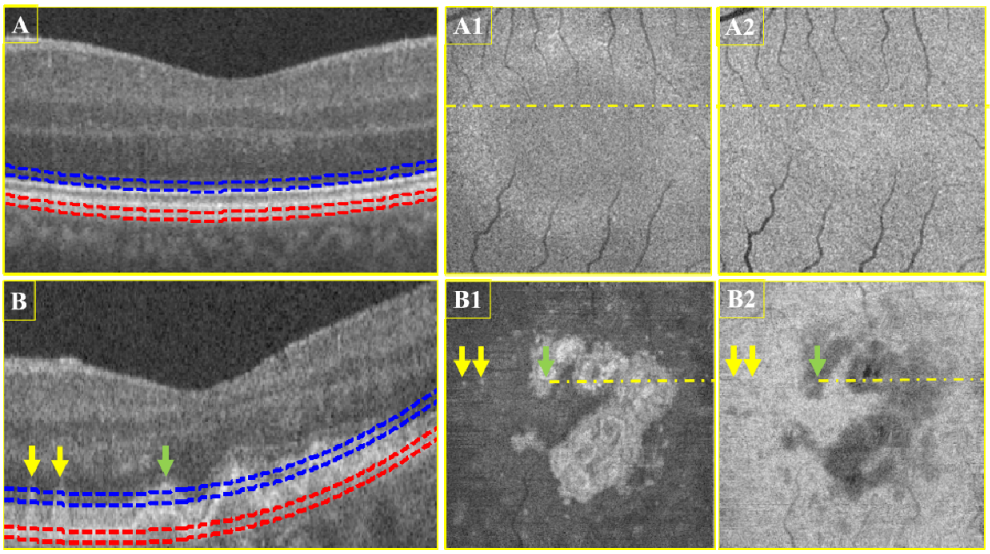

Fig. 3. Drusen visualization of C-scans contained in two slabs at different depths. (A) B-scan of a normal eye (B) B-scan of an eye with dry AMD containing soft drusen and subretinal drusenoid deposits. (A1, B1) The innermost C-scan contained in the blue slab. Drusen area appears hyper-reflective compared to the background in (B1). (A2, B2) The outermost C-scan contained in the red slab. Soft drusen areas and vessel shadows appear hypo-reflective compared to the background in (B2) but subretinal drusenoid deposits are only evident in the blue slab. Yellow dashed lines indicate the position of the representative B-scans. Green arrows indicate soft drusen positions and yellow arrows indicate subretinal drusenoid deposits.

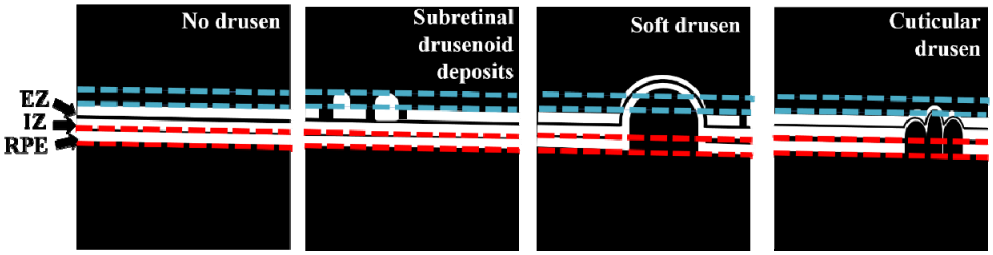

Fig. 4. Representation of how three types of drusen are observed in each slab. Inner slab (blue) is located right above the ellipsoid zone (EZ) interface, and only appears bright in the event of drusen. If the outer boundary of RPE in a soft drusen region is above the inner slab, a black region surrounded by bright pixels is observed. The outer slab (red) appears normal in the event of subretinal drusenoid deposits because they locate above the RPE, and dark for other types of drusen. IZ – Interdigitation zone.

Then, a hybrid contrast map similar to the generated in Ref [51]. was performed as an initial diagnosis step to separate scans containing drusen from those without. First, the averaged reflectance of the seven C-scans forming each slab was calculated and normalized. Then we computed the global contrast of *en face* reflectance image (Eq. (1) as well as the local contrast (LC) between pixels and their immediate surroundings (Eq. (2),

$$GC(x,y) = \frac{I(x,y)}{mean(I)} \tag{1}$$

$$LC(x,y) = \frac{w^c(x,y)}{w^s(x,y)} \tag{2}$$

Biomedical Optics EXPRESS

where w^c is the average intensity within a central circle at (x, y) with a diameter of 60 μm, and w^s is the average intensity of the surrounding ring with an inner diameter of 60 μm and outer diameter of 130 μm. A hybrid contrast map was generated for each of the two projected slabs by multiplying the global and local contrasts at each pixel. Then, the maximum value of the two contrast maps were found and averaged. A threshold to identify healthy retina from that containing drusen could be easily determined (Fig. 5).

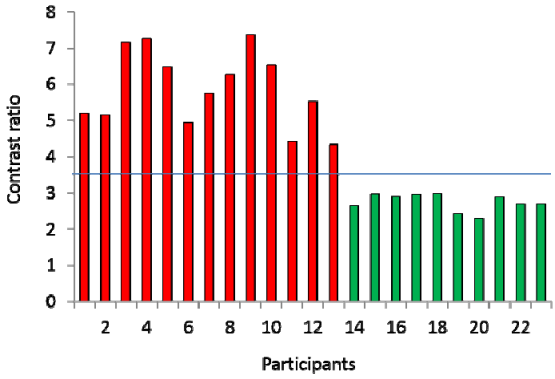

Fig. 5. The bar graph of mean maximum hybrid contrast ratio in a scan of each participant. Thirteen participants were imaged in each group. A threshold at 3.5 can completely separate the normal eyes (green bars) and the drusen eyes (red bars).

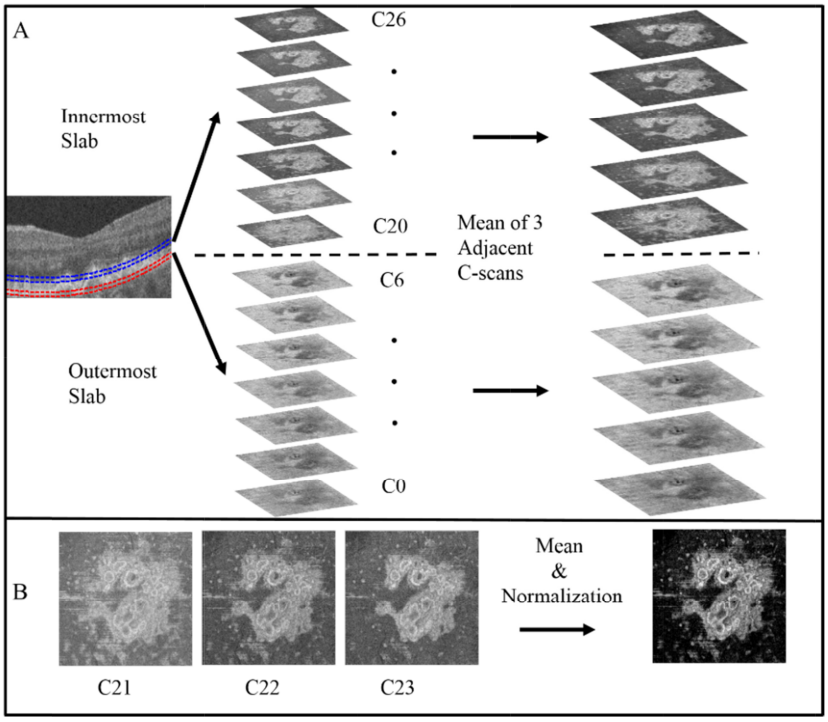

Fig. 6. 3D mean filter indicated in operation 6 of Fig. 2. Panel (A) describes the steps followed. Each slab contains seven consecutive C-scans, each containing the reflectance data at a different distance from the Bruch's membrane. Every trio of adjacent C-scans is averaged, resulting in five averaged C-scans per slab. Panel B shows an example of one trio of adjacent C-scans from the inner slab containing drusen, before and after averaging and normalization.

Biomedical Optics EXPRESS

In the first processing step, averaging groups of three adjacent C-scans (Fig. 6) along seven depths within each slab generates five *en face* images with enhanced contrast between drusen area and background. The reflectance values of the resulting averaged *en face* images were normalized to values between 0 and 1 and passed to the next processing step.

3.3 Drusen segmentation

The combination of Top-Hat transform and Otsu thresholding has been used before on medical image segmentation using grayscale images with uneven illumination [52]. In this step, they are implemented to detect drusen in each of the averaged *en face* images contained in each slab. The Top-Hat transform operates by extracting elements of the input image that are smaller than a pre-defined structuring element and are brighter than their surroundings. Therefore, the dark areas in the outer slab were inversed, since the Top-Hat transform is only suitable for bright objects. For each of the five averaged *en face* images in each slab, the transform was applied twice using structuring elements with dual scales (disks of radii 60 and 15 pixels) followed by Otsu thresholding. Then, a logical OR between the two outputs corresponding to different disk scales was applied, followed by median filtering to generate five drusen maps in each slab. Generation of one drusen map in the inner slab is shown in Fig. 7. By applying a dual-scale approach, both large drusen and small drusen can remain in the *en face* drusen maps.

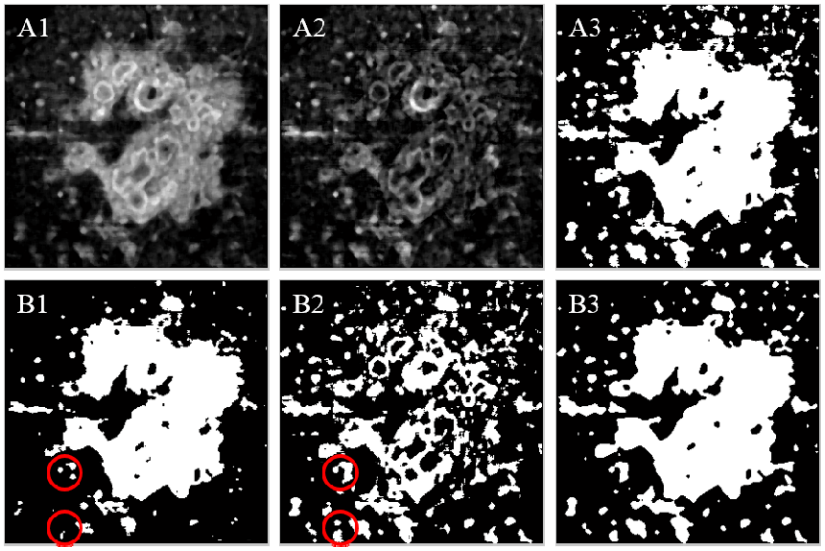

Fig. 7. Dual-scale filtering step. (A1) The averaged C-scan obtained in Fig. 6(B) was processed by a 5 × 5 median filter and Top-Hat transform (disk of radius 60 pixels). (B1) The binary image of (A1) after Otsu thresholding. (A2) The same processing in (A1) but using a disk of radius 15 pixels. (B2) The binary image of (A2) after Otsu thresholding. The areas enclosed by red circles are examples of regions detected in (B2) better than in (B1). (A3) The combination of (B1) and (B2) by a logical OR. (B3) The binary image (A3) after filtering by 5 × 5 median filter.

At this point, ten binary images (five per slab) equivalent to the one shown in Fig. 7(B3) have been generated. To refine the drusen detection a continuity examination routine followed. A 9 × 9 pixel window was moved along the binary images with one pixel step in each axis. Within the window at each position, the Jaccard similarity metric between the windows W_1 and W_2 of two axially adjacent binary images was computed, defined in Eq. (3). Jaccard similarity coefficient values range from 0 to 1. Every position that had a coefficient larger than 0.5 was set to one while positions with values lower than that were filtered out (Fig. 8). The output of the continuity examination step was four binary images per slab. At

Biomedical Optics EXPRESS

each slab these four images were added and pixels with value larger than 2 were set to 1 while the remaining pixels were set to zero.

$$J = \left| \frac{W_1 \cap W_2}{W_1 \cup W_2} \right| \tag{3}$$

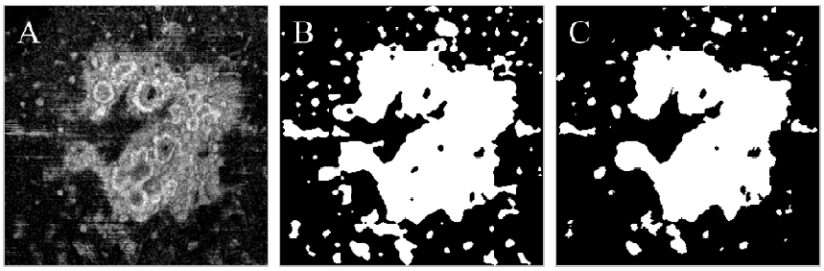

Fig. 8. (A) An averaged C-scan corresponding to the inner slab. (B) One of the five binary images in the inner slab. (C) The inner slab mask after continuity detection.

3.4 Post-processing step

At this point, the inner slab has detected most of the drusen area, but its mask is still dark at the locations where elevation of the RPE is too high. The outer slab has detected most of the soft drusen area (Fig. 9(A1)-9(A2)), small dark regions under drusen where RPE does not exhibit significant elevation (Fig. 9(D)-9(E)) and shadows from large vessel in the inner retina. In order to remove shadow artifacts, an opening operation with disk size equal to seven pixels was performed. Then, a logical OR between the binary masks of both slabs (Fig. 9(A2)-9(B2) followed by an additional median filter step generated the definitive drusen area map (Fig. 9(C).

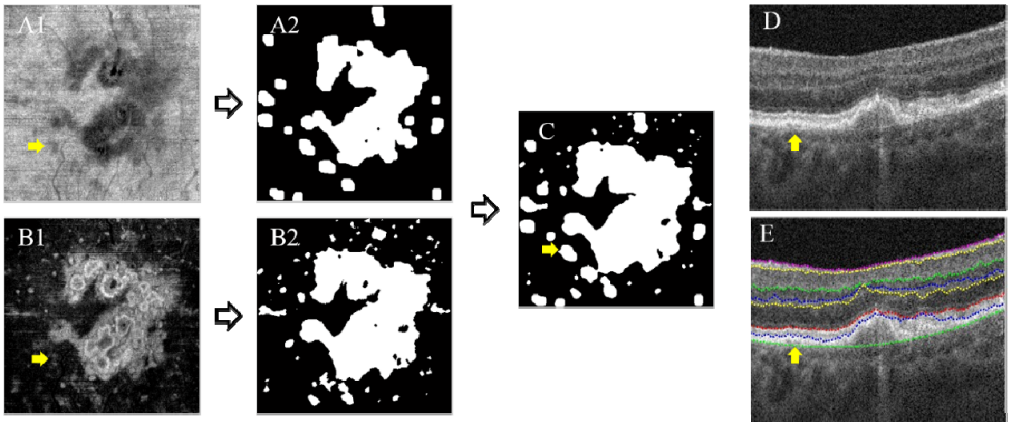

Fig. 9. Post processing step. (A1) Average of C-scans in the outer slab. (A2) Outer slab mask after large vessel shadow removal and continuity detection. (B1) Average of C-scans in the inner slab. (B2) Drusen mask of the inner slab (same as Fig. 8(C)). (C) The final segmentation result. (D) A representative B-scan showing a large soft drusen region to the right of a small drusen region (indicated by a yellow arrow) that does not significantly elevates the RPE (E) and is better detected by the outer slab in A1-A2.

4. Evaluation

To assess the accuracy and robustness of the proposed method, we evaluated the repeatability of the calculated drusen area and compared our drusen segmentation results *en face* with results from cross-sectional manual RPE delineation on twenty randomly selected B-scans per volume. For manual delineation the drusen boundary was contoured by two experienced

Biomedical Optics EXPRESS

graders (AH and YL) and the results were compared to automated detection by computing the true positive area fraction (TPAF), false positive area fraction (FPVF), accuracy rate (ACC) and Dice similarity coefficient (DSC). TPAF indicates the rate of correctly detected area (Eq. (4), where A_{TP} denotes the true positive set and A_{MG} the area calculated from manual grading. FPAF denotes the fraction of incorrectly detected area (Eq. (5), where A_{FP} indicates the set of false positives and A is the total area. ACC indicates the detection accuracy rate (Eq. (6), where A_{TN} is the set of true negatives. DSC is used for comparing the similarity between the automated segmentation results and manual grading (Eq. (7), where A_a and A_m are the drusen areas detected by a grader and by the automatic drusen detection algorithm respectively; and $A_{a\cap m}$ is the drusen detected by both methods.

$$TPAF = \frac{A_{TP}}{A_{MG}} \tag{4}$$

$$FPAF = \frac{A_{FP}}{A - A_{MG}} \tag{5}$$

$$ACC = \frac{A_{TP} + A_{TN}}{A} \tag{6}$$

$$DSC = \left| \frac{2 \times A_{a\cap m}}{A_a + A_m} \right| \tag{7}$$

Data from one eye of 13 participants with drusen was collected and analyzed. All three types of drusen could be detected (Fig. 10) and the average running time was 22 seconds. The signal strength index (SSI) of the scans used for this study was 63 ± 7 and those with signal strength index lower than 55 were still rejected, as recommended by the manufacturer. Excellent repeatability was observed between two consecutive volumetric scans of each eye, resulting in a coefficient of variation of 6.4%. The results of the evaluation metrics described above are summarized in Table 1.

Biomedical Optics EXPRESS

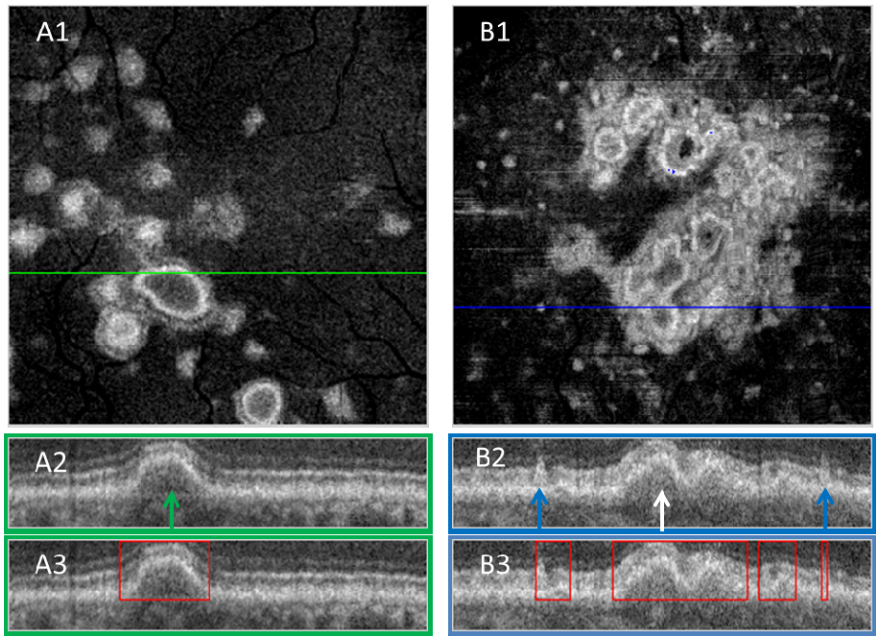

Fig. 10. Demonstration of three types of drusen detected by the algorithm in two dry AMD cases. (A1, B1) en face images representing the mean of C-scans in the inner slab. (A2, B2) representative B-scans. Soft drusen observed as an isolated structure with significant RPE elevation is indicated by a green arrow in A2. Subretinal drusenoid deposits above the intact RPE are indicated by blue arrows in B2. A white arrow in B2 indicates cuticular drusen, evidenced by its saw-tooth appearance connected to adjacent structures. (A3, B3) the drusen regions automatically detected by the algorithm.

Table 1. Comparison of drusen area between automatic segmentation and manual grading by certified graders AMH and YL.*

	TPAF (%)	FPAF (%)	ACC (%)	DSC (%)
YL	82.78 ± 5.91	3.15 ± 1.98	90.54 ± 2.83	88.95 ± 3.45
AMH	73.72 ± 6.93	2.66 ± 2.74	85.22 ± 3.92	83.84 ± 4.28

* Mean ± standard deviation

Overlapping between the manual and automatic drusen segmentation was also visually investigated. A certified grader identified the A-line positions affected by drusen in 152 alternating B-scans on two cases and the missing frame was interpolated. Morphological opening smoothed the boundaries of the manual segmentation after interpolation. Good agreement between the two was observed (Fig. 11).

Biomedical Optics EXPRESS

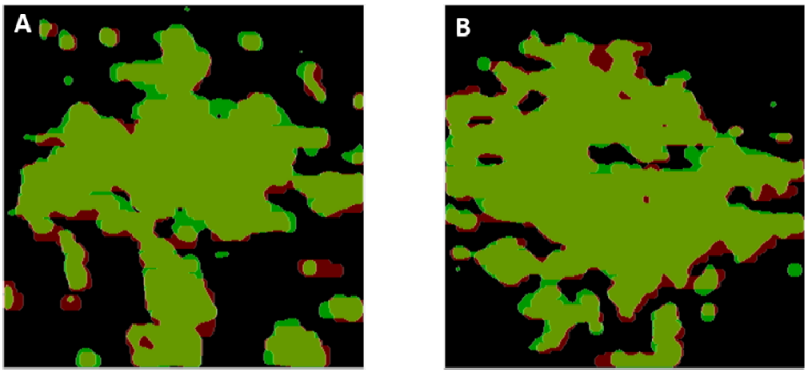

Fig. 11. Overlap between manually segmented drusen after interpolating missing frames and morphological opening vs automatically detected drusen in two scans. Yellow region represents overlapping areas, red region represents areas detected only by manual segmentation and green regions represent areas detected by automatic segmentation only.

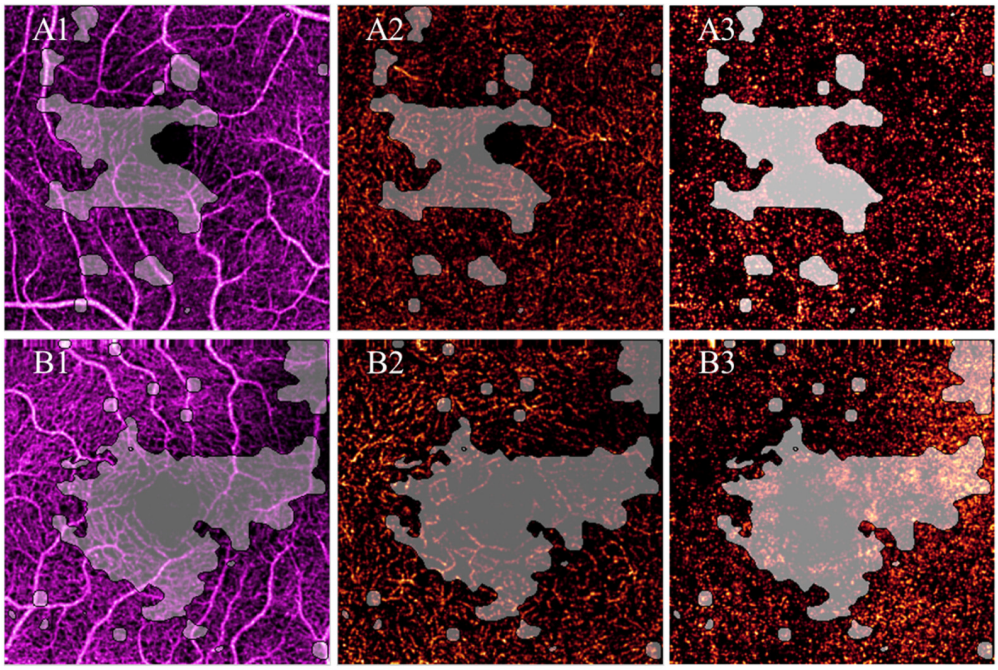

Fig. 12. Drusen area (gray) overlaid on *en face* angiograms. A1,A2 show the drusen detected by the current algorithm overlaid on the inner retinal angiogram. B1, B2 show the drusen overlaid on the deep plexus angiogram. A3, B3 show the drusen overlaid on the choriocapillaris angiogram.

The scanning protocol utilized allowed to process the OCT signal and generate depth-resolved *en face* OCT angiography (OCTA) of the retina. The split-spectrum amplitude decorrelation angiography (SSADA) algorithm was used to generate the flow data [53], motion correction technology [48, 49, 54] was used to remove motion artifacts and a projection-resolved algorithm [55] was applied to remove projection artifacts cast by superficial flow onto deeper layers. The inner retina was defined as the slab between the inner limiting membrane (ILM) and the outer plexiform layer (OPL), the deep plexus was defined as the flow within the OPL and the choriocapillaris was a slab of about 10 μm thickness below the Bruch's membrane [56]. Angiograms were generated by maximum projection of

Biomedical Optics EXPRESS

the flow data within the slab [57]. Then, the drusen area detected could be represented in tandem with the *en face* angiography information (Fig. 12) and the potential relationship between drusen area and capillary perfusion could be visualized.

5. Discussion and conclusion

This report demonstrates a novel method to automatically detect the area of all types of drusen, which is detected by OCT without the need for segmentation of the inner boundary of RPE. The algorithm is based on depth-resolved analysis of C-scans within two slabs located at different depths above the Bruch's membrane. The inner slab detects subretinal drusenoid deposits, while the outer slab detects soft drusen and cuticular drusen. The challenging type of subretinal drusenoid deposits had been detected by multi-modal methods previously [58–61], but detection by OCT alone had not been previously demonstrated. The method exhibits good detection accuracy and repeatability.

Methods to detect drusen that rely on the segmentation of irregular RPE are confronted with two separate challenges. First, small drusen deposits require highly-sensitive detection techniques and second, segmentation errors need to be avoided at the inner boundary of RPE. Disadvantages of algorithms that analyze elevation maps from segmentation results can be summarized as: (1) The segmentation based on graph search often fails on drusen with abrupt elevation, because the gradients between layers are not smoothly connected and searching for a neighboring pixel with the lowest connection cost is not very reliable [41, 62]. In addition, it is common for graph search segmentation algorithms to intentionally neglect small reflectance changes in the definition of cost functions, considering the effect of speckle noise. (2) The segmentation fails due to reflectance variance caused by shadows of large vessels, media opacity or pupil vignetting [63]. (3) The threshold height used to discern whether there is a substantial RPE line deviation from the "healthy" baseline (and hence account for the presence of drusen) is arbitrary, not based on histological findings and limited by the axial resolution of the OCT system.

In this work, by using multiple-depth C-scan, we have circumvented the sources of failures or inaccuracy listed above. The reflectance on C-scan is the contrast we used to distinguish drusen from normal retinal tissue. The reflectivity change due to the onset of drusen formation (microstructural changes) should be much earlier than the production of substantial RPE elevation. As a result, the early drusen can be discerned by the methods based on reflectivity like ours, while often ignored by the methods based on layer changes.

Speckle noise is inherent to both *en face* and cross-sectional images due to the interferometric nature of the OCT technology, and could lead to an increment of false positive pixels. Although this type of noise can be reduced by averaging successive scans at the same position, long scanning procedures are not a desirable approach when imaging diseased eyes. In our method, we prevent inaccuracies associated with speckle noise outside the drusen area by averaging across consecutive C-scans in a slab and a continuity detection routine.

A pathology that affects the older population such as AMD is often associated with reduced eye transparency such as cataract, which contributes to lower signal strength scans and consequently lower layer contrast. Consequently, any method that attempts to measure drusen area has to exhibit good performance in low quality scans. While there is no method that reduces the high reliance of B-scan segmentation performance on fine layer contrast, there are many validated and well-established methods that can be used on *en face* images to accurately and reliably separate groups of pixels of different reflectance in order to detect atrophy areas. For this reason, our method appears more robust than those relying on retinal layer segmentation.

Next, we briefly discuss an assumption that might affect the accurate evaluation of individual cases. Due to population variations of the outer retinal thickness, the relative position of the inner slab with respect to the EZ layer will vary. This method is sensitive to the EZ layer falling into the inner slab, therefore we set the slab's outer boundary at the mean

Biomedical Optics EXPRESS

value of the EZ-Bruch's membrane distance found in the set of healthy subjects (20 pixels), assuming that the healthy part of diseased eyes is less likely to exhibit larger thickness than in healthy eyes. The continuity routine performed in step 10 of Fig. 2 is in charge of excluding from detection the positions of healthy tissue with EZ layer just reaching the outermost C-scans of the inner slab. The good agreement with manual graders suggests that although sensitivity to eyes with large deviations with respect to the standard are unavoidable, the method is otherwise very robust to the majority of subjects.

The running time we have reported is mainly the cost of the Bruch's membrane semi-automatic segmentation step. Our method still involves segmentation of this boundary, but it should be noted that Bruch's membrane preserves its shape even in the presence of drusen or other pathologies. For this reason, segmentation of the Bruch's membrane is a relatively simple task [64] and therefore, our algorithm can perform its layer segmentation routine much faster and more accurately than those relying on semi-automatic segmentation of the pathologic RPE's inner boundary.

Histological studies have reported choriocapillaries dropout in regions underlying drusen [65]. However, the relationship between drusen area and perfusion of the inner-retinal/deep plexus, which lies above the drusen, remains unclear [66, 67]. Since the data acquired here allows to simultaneously generate depth-resolved *en face* angiograms and a drusen map, as well as computation of the drusen area and the vessel density, it might be of interest to future investigations in the field of OCTA. Additionally, this technique may allow assessing if choriocapillaris flow can be detected under certain types of drusen.

Finally, the main limitation of this work is that although a 3D technique is used and depth-resolved information is exploited to detect drusen, volumetric quantification of drusen size is not possible.

In summary, an accurate and automated drusen detection algorithm is proposed, based on multiple-depth C-scan analysis. By using this approach, we prevent inaccuracies caused by errors in the segmentation of the pathologic RPE and avoid tedious manual correction. The technique requires minimal operator effort since it only relies on delineating the Bruch's membrane interface. Its capability to measure cuticular drusen and subretinal drusenoid deposits constitute an advantage over the majority of segmentation-based techniques that can only detect drusen that results in significant elevation of the RPE. This drusen detection method appears to allow earlier detection of this indicator of AMD progression in asymptomatic subjects.

Funding

This work was supported by grants R01 EY024544, R01EY027833, DP3 DK104397, P30 EY010572 from the National Institutes of Health (Bethesda, MD), National Natural Science Foundation of China (NO. 61471226), Natural Science Foundation for Distinguished Young Scholars of Shandong Province (NO. JQ201516), China Scholarship Council, China (grant no.: 201608370107) and an unrestricted departmental funding grant and William & Mary Greve Special Scholar Award from Research to Prevent Blindness (New York, NY). The authors also thank the supporting of Taishan scholar project of Shandong Province.

Financial disclosure

Oregon Health & Science University (OHSU), Yali Jia, and David Huang have a significant financial interest in Optovue, Inc. These potential conflicts of interest have been reviewed and managed by OHSU.